Wyszkowska, E.; Mieszczynski, C.; Kurpaska; Azarov, A.; Chromiński, W.; Jóźwik, I.; Esfandiarpour, A.; Kosińska, A.; Kalita, D.; Diduszko, R.; Jagielski, J.; Nori, S. T.; Alava, M.

The Fe addition as an effective treatment for improving the radiation resistance of fcc Ni_xFe_{1-x} single-crystal alloys

Published in:
Journal of Nuclear Materials

DOI:
10.1016/j.jnucmat.2023.154565

Published: 01/10/2023

Document Version
Publisher's PDF, also known as Version of record

Journal of Nuclear Materials 584 (2023) 154565

Contents lists available at ScienceDirect

Journal of Nuclear Materials

journal homepage: www.elsevier.com/locate/jnucmat

The Fe addition as an effective treatment for improving the radiation resistance of *fcc* Ni_xFe_{1-x} single-crystal alloys

E. Wyszkowska [a,*], C. Mieszczynski [a], Ł. Kurpaska [a], A. Azarov [b], W. Chromiński [a,c], I. Jóźwik [a,d], A. Esfandiarpour [a], A. Kosińska [a], D. Kalita [a], R. Diduszko [a], J. Jagielski [a,d], S.T. Nori [a], M. Alava [a,e]

[a] National Centre for Nuclear Research, NOMATEN CoE MAB+, Andrzeja Soltana 7, 05-400 Otwock-Swierk, Poland,
[b] Centre for Materials Science and Nanotechnology, University of Oslo, PO Box 1048 Blindern, N-0316 Oslo, Norway
[c] Warsaw University of Technology, Faculty of Materials Science and Engineering, Wołoska 141, 02-507 Warsaw, Poland
[d] Łukasiewicz Research Network – Institute of Microelectronics and Photonics, Al. Lotników 32/46, Warsaw, Poland
[e] Department of Applied Physics, Aalto University, P.O. Box 11000, 00076 Aalto, Espoo, Finland

HIGHLIGHTS

- Defect type and density influence the shape and intensity of the RBS/C spectra.
- A rapid increase in the number of defects at 0.5 dpa was observed for all alloys.
- $L1_2$ nanoprecipitates could be behind the highest hardness of $Ni_{0.62}Fe_{0.38}$.

ARTICLE INFO

Keywords:
Nanoindentation
fcc Ni_xFe_{1-x} single crystals
TEM, Ion channeling
MC/MD simulations

ABSTRACT

In this work, five different compositions of *fcc* Ni and Ni_xFe_{1-x} single crystal alloys namely Ni, $Ni_{0.88}Fe_{0.12}$, $Ni_{0.77}Fe_{0.23}$, $Ni_{0.62}Fe_{0.38}$, $Ni_{0.38}Fe_{0.62}$ were irradiated by 1.5 MeV ^{58}Ni ions at room temperature in a wide fluence range (4×10^{13} to 4×10^{15} ions/cm^2). The role of Fe addition on the radiation resistance of the Ni_xFe_{1-x} single crystals was studied by transmission electron microscopy (TEM), ion channeling technique (RBS/C) and nano-indentation techniques. The Multi-Step Damage Accumulation analysis revealed the cross-sections for damage formation significantly decreases for $Ni_{0.38}Fe_{0.62}$ and $Ni_{0.62}Fe_{0.38}$ as compared to that in pure Ni single crystal, which is consistent with RBS/C and TEM results. The results of nanoindentation show that $Ni_{0.62}Fe_{0.38}$ alloy possesses the highest hardness (2.96 GPa) among the other compositions in a pristine state. To interpret this result, hybrid Monte Carlo/ Molecular dynamics simulations were used to check the presence of the ordered crystal phase structure for Ni_xFe_{1-x} binary alloys. The simulation results have shown that depending on the iron content, we deal with different amounts of $FeNi_3$ ($L1_2$) phase. This result revealed that in $Ni_{0.62}Fe_{0.38}$ alloy, nanoprecipitate $FeNi_3$ ($L1_2$) phase (around 20%) is formed inside the disordered matrix, which could be one of the main reasons for the high hardness of this alloy before irradiation.

Additionally, we have found adding iron reduced the number and size of the defects (as a result of ion irradiation) in Ni_xFe_{1-x} because the Fe element is more stable than Ni, which results from the electron configuration of both elements in the excited state. Therefore, the more iron in the material, the fewer defects are created.

1. Introduction

Structural materials for the next generation fission reactors must meet various requirements to ensure their safe operation. In particular, the radiation resistance of such materials is essential. Radiation damage in crystalline materials has been studied extensively for decades [1]. This has been originally motivated to control neutron irradiation-induced degradation of fission reactor materials. The macroscopic material degradation is fundamentally a manifestation of the evolution of the radiation damage-induced defects. Three processes

* Corresponding author.
E-mail address: edyta.wyszkowska@ncbj.gov.pl (E. Wyszkowska).

https://doi.org/10.1016/j.jnucmat.2023.154565
Received 28 February 2023; Received in revised form 13 May 2023; Accepted 6 June 2023
Available online 7 June 2023

can describe the evolution of radiation-induced defect concentrations in metals across the primary and secondary damage stages: (a) defect production from atomic collision cascades; (b) consecutive vacancy-interstitial recombination; and (c) point defect absorption by different types of sinks like dislocations and grain and phase boundaries [2]. The point defects that survive recombination and sink absorption may cause different effects. For example in the case of surrogate irradiation via heavy ions, defects may migrate both into the bulk material and to the surface at a high level of mechanical stress induced by ion irradiation. This can result in an extended damage region due to enhanced defect migration with increasing ion fluence. Thus, point defects can diffuse and subsequently generate dislocation loops [3] and stacking fault tetrahedrons (SFT) under the stress gradient, depending on the material.

Additionally, the formation of large vacancy clusters significantly worsens the performance of materials, as vacancies may lead to void swelling. Therefore, controlling vacancy migration and effectively annihilating vacancies is crucial in selecting new advanced structural materials for nuclear applications [4–6]. Thus, it is critical to understand the defect dynamics; however, research focused on enhancing defect recombination and controlling defect migration [7] in metallic alloys is meager. There is evidence that tuning the chemical composition of a single-phase alloy may significantly change the features of defect clusters [3], which needs to be elaborated. Furthermore, the defect clusters may lead to macroscopically observable degradation effects, such as irradiation hardening, embrittlement, and irradiation-induced creep. These phenomena adversely affect materials used in advanced Generation IV fission and fusion reactors. This is because the materials are subjected to harsh operating conditions such as temperatures in excess of 600 °C, high radiation fluences (around 50 displacements per atom (dpa)), high-mechanical stresses, and corrosive environments [8–10]. Conventional metal alloys such as ferritic and austenitic stainless steel fail under such reactor conditions due to the effects mentioned above. Thus, the selection of new materials needs special attention for high radiation tolerance in a wide fluence range, high thermal and phase stabilities, and good mechanical properties [4]. Despite that materials for advanced reactors have been intensively studied during the past decade [5,8,11–15]; there is still an emerging research field with great scope for exploration. Hence, in the present work, we focus on the investigation of novel metallic alloys for advanced nuclear reactor structural material applications and their assessment to understand defect dynamics and mechanical properties.

The new class of single-phase concentrated solid solution alloys (CSAs), including high entropy alloys (HEAs), exhibits remarkable mechanical, chemical, and magnetic properties, including high yield strength, fracture toughness, wear resistance, and corrosion resistance, compared to conventional alloys [16–21]. The Ni_xFe_{1-x} (x= atomic percentage of Ni) single crystal alloys are promising materials, which can withstand demanding environments, such as the structural materials for nuclear applications where high radiation tolerance is of primary concern [4–6]. Understanding the irradiation response and material degradation level is still a great challenge especially the urgent analysis is necessary for initial damages up to 1 dpa and higher damages of the order of 10 or even 20 dpa [9,10]. Initial studies of Ni_xFe_{1-x} alloys have demonstrated the formation of dislocation loops and stacking fault tetrahedral defects [2–6,8,22]. Therefore, the proposed work would launch a state-of-the-art examination of Ni and Ni_xFe_{1-x} single crystal alloys. These are promising materials due to their extraordinary mechanical properties and high radiation tolerance related to simple structure, Fe element and lack of grain boundaries [2–6,8,22].

In the present work, we use Rutherford backscattering/-channeling spectrometry (RBS/C) for qualitative evaluation of radiation damage or the Multi-Step Damage Accumulation (MSDA) analysis to reveal damage kinetics for each of the proposed compositions. The RBS/C technique allows for assessing the radiation damage level for different compositions in various fluences [23,24]. In addition, the defect sizes and densities were studied with Transmission Electron Microscopy (TEM) in Ni_xFe_{1-x} single crystals. The nanoindentation technique was used to record mechanical properties such as hardness as a function of irradiation fluence and Fe concentration. Nanoindentation of irradiated materials is an emerging research avenue with inadequate understanding, and our research could contribute to its development. Moreover, the presence of the ordered crystal phase structure for Ni_xFe_{1-x} binary alloys by using atomistic simulation has been checked by performing hybrid Monte Carlo/ Molecular dynamics simulations.

In general in our research, we are conducting a parametric study individually for Fe addition, temperature, and irradiation dose. In the current work, we focus on Fe addition and irradiation dose; thus, the Fe implantation was conducted at room temperature. Moreover, since the defect density is relatively less and the defects are rather less mobile at room temperature, it provides an opportunity to understand the defect formation and evolution better via combining experimental and modeling efforts.

2. Material and methods

2.1. Material production and sample preparation

The *fcc* Ni and Ni_xFe_{1-x} single crystal alloys with different amounts of Fe (12, 23, 38 and 62 at%) were produced at NCBJ [25] using the vertical temperature gradient method (also called the Bridgman method [26]). In this method, metals with high melting temperatures, such as Ni and Fe, are melted and crystallized in an alundum crucible in an Ar gas protective atmosphere using a Mo wire heating element. The crystallization process utilized a slow lowering rate of ~1 to 2 cm/hour of the crucible, delivering one single crystal per ~30 h. Samples were then cut along [001] direction, ground, and polished before ion irradiation. Firstly, mechanical grinding was performed using abrasive papers with grit sizes from 400 to 4000. Secondly, polishing to a mirror-like surface finish was achieved using diamond pastes with a grain size of 6 μm, 3 μm, and 0.5 μm and subsequent electro-polishing (Struers LectroPol-5) with 60% Perchloric acid electrolyte to reduce stresses generated by mechanical polishing. The electro-polishing time was set to 60 s and an electric potential of 30 V.

2.2. Ion irradiation

All the specimens produced and prepared per the methodology mentioned in 2.1 were subjected to ion irradiation according to the parameters obtained by SRIM code [27] simulation (predicted damage depth, ions, energy). The irradiations were carried out at room temperature with 1.5 MeV $_{58}Ni^{+}$ ions using a 1 MV tandem accelerator (National Electrostatics Corporation, model 3SDH-2) in the University of Oslo. All ion irradiations were performed in a raster scanning mode. The beam current was kept constant at a relatively low value of ~50 nA/cm^2 corresponding to the ion flux of ~3e11 at/cm^{2}s, to avoid sample heating during implantation. The Ni^{+} ions were chosen for irradiation because Ni is one of the major alloying elements in the Ni_xFe_{1-x} system. Therefore, there is no introduction of impurities during radiation damage buildup. Furthermore, in structural materials, there is an SIA cluster evolution bias due to their higher migration rate compared to vacancy clusters under irradiation. Self-ion implantation (Ni in this case) can further enhance this bias; however, the concentration of Ni ions implanted is insignificant compared to the SIAs created due to the radiation damage event. Thus, self-ion-induced defect evolution can emulate neutron irradiation effects albeit slower due to room temperature effect. The irradiations were performed at an inclination of 7° to the normal direction of the samples to avoid channeling.

The corresponding displacement per atom (dpa) profiles were predicted by the SRIM code for all elements using the full cascade mode. The dpa has been calculated based on the following equation according to recommendations of [28,29]:

dpa=[fluence (ions/cm^2)×total vacancies/A-ion × 10^8] /atomic density (atoms/cm^3) (1)

The mean projected ranges of ions and induced defect distributions (estimated by SRIM simulations [29,30]) for Ni and $Ni_{0.38}Fe_{0.62}$ are shown in Fig. 1A and B.

The ion distribution was estimated from the RANGE.txt file. The corresponding dpa profiles were calculated using two files, VACANCY.txt and NOVAC.txt, under an assumed displacement energy threshold of 40 eV for all elements. The dpa profile is the sum of the vacancy concentrations using the column of "Knock-Ons" for Ni ions and the columns of "Vacancies" from target elements (the sum of Ni vacancies and Fe vacancies in the case of Ni_xFe_{1-x}) in VACANCY.txt, together with the replacement collisions in NOVAC.txt. [31]. Ion-induced damage in monoatomic and multielemental targets was predicted using full-cascade simulations [29,30]. The SRIM-estimated damage peak is located at a depth of approximately 400 nm.

2.3. RBS/C (ion channeling) and MSDA model

After irradiation, the samples were examined by the RBS/C using 1.6 MeV He^+ ions along the [001] direction and backscattered into a detector placed at 165° relative to the incident beam direction. RBS/C measurements were performed using 1 MV tandem accelerator (National Electrostatics Corporation, model 3SDH-2) in the University of Oslo. The RBS/C spectra for pure Ni and Ni_xFe_{1-x} alloys irradiated with different fluences were simulated using the Monte Carlo McChasy code developed at the NCBJ [30,32]. The energy of the backscattered particle can be directly related to the depth at which the close encounter scattering event occurred. The bulk scattering arises from particles that have been deflected atomic rows and have crossed over to another row, where they undergo a close-encounter event. To reveal the damage kinetics for investigated alloys the Multi-Step Damage Accumulation (MSDA) analysis was performed [33,34]. This model is based on the equation assuming that the damage accumulation occurs through a series of structural transformations caused by the destabilization of the present crystal structure.

2.4. Hybrid MC/MD simulation

The possibility of formation of the ordered crystal phases was verified for Ni_xFe_{1-x} binary alloys by using hybrid Monte Carlo/ Molecular dynamics (MC/MD) atomistic simulation. We start the simulation with a random distribution of Ni and Fe atoms in the matrix for each Ni_xFe_{1-x} alloy. Such a random distribution cannot necessarily reproduce thermodynamically stable local atomic structure and hence, the simulations reveal an equilibrated stable system with the least potential energies. The hybrid MC/MD algorithm [35,36] was employed to facilitate thermally induced kinetics and anneal each alloy system. To perform such a simulation, we utilized LAMMPS [37] and modified embedded atom method (MEAM) interatomic potential [38], which reproduced the phase diagrams of Ni_xFe_{1-x} binary alloys. For each composition, a simulation cell with *fcc* crystal and random distribution of constituent elements was created containing 32,000 atoms. Periodic boundary conditions are applied in all three directions. After minimization of each system using the conjugate gradient algorithm, it is equilibrated at 300 K using the NPT ensemble. We used the following hybrid MC/MD steps [36]:

1. Two different atom types (Fe and Ni) are selected randomly in the simulations and tried to swap the position so that the kinetic energy keeps constant by swapping.
2. Metropolis criterion is used and each swap attempt is accepted if $\epsilon < \frac{P_f}{P_i}$, where ϵ is a random number between [0,1] and $P_i = e^{-\beta U_i}$, where β is the inverse of k_BT and U_i is the potential energy of the system. Swapping is tried 200 times.
3. To relax any local residual stress induced by swapping, 50 molecular dynamic time steps under constant pressure (NPT) conditions are performed.

We repeat these three steps until we reach reasonable convergence of the system's potential energy. The ordered crystal structures are analyzed using a polyhedral template matching algorithm [39] that is implemented in OVITO software [40].

2.5. Nanoindentation

Nanoindentation was performed utilizing the Micro Materials Ltd NanoTest Vantage system using a Synton-MDP diamond Berkovich-shaped indenter. The preliminary tests were conducted in multiple load cycles with increasing load from 0.5 mN up to 10 mN (in total ten cycles) using load controlled method. At least 16 indentations were made at each load with 50 μm spacing between the indents. Before starting the indentation campaign, a Diamond Area Function (DAF) of the indenter tip is calculated. The calibration is performed using Fused Silica material in a wide load range to assess a reliable indenter shape for a given indentation depth.

2.6. TEM analysis

Suitable electron transparent lamellae were prepared from the area of interest of the samples via a focused ion beam/scanning electron microscope (FIB/SEM) for TEM microstructural studies. A lift-out procedure was utilized in FIB (Ga+) installed in Helios 5 UX (ThermoFisher Scientific) microscope at NCBJ. Final thinning of the lamellae was performed with 5 keV Ga^+ ions followed by 2 keV Ga+ gentle polishing. TEM observations were performed with the JEOL JEM1200EX II

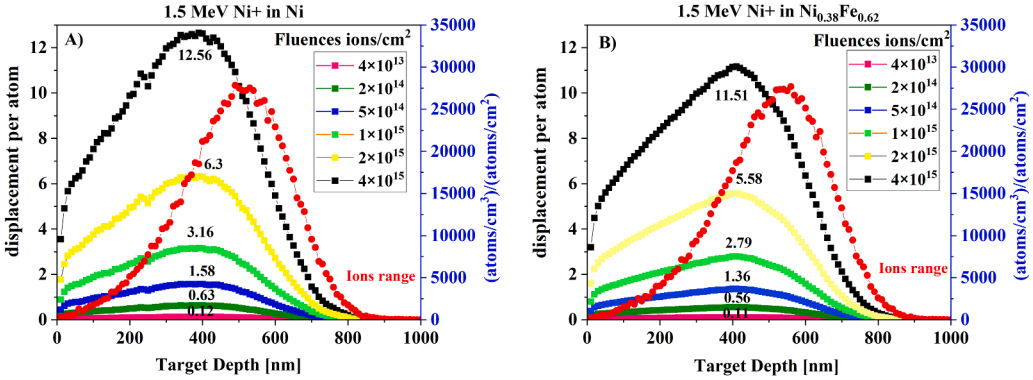

Fig. 1. Damage profiles of (A) Ni and (B) $Ni_{0.38}Fe_{0.62}$ irradiated with 1.5 MeV of Ni+ at fluences of 4×10^{13}, 2×10^{14}, 5×10^{14}, 1×10^{15}, 2×10^{15}, and 4×10^{15} ions/cm^2.

microscope operated at 120 kV. Since ion irradiation is depth-dependent, evaluating the damage distribution below the sample surface induced by ion irradiation is crucial. All the lamellae have been cut perpendicularly to the ion irradiated surface to reveal the damage distribution into material up to the 2 um depth. Afterward, images of the most degraded regions have been taken at 500k magnification to perform a detailed analysis of the type of the defects, sizes and calculate the defect densities. The two-beam convergent beam electron diffraction technique was used to determine lamellae thickness (for dislocation density statistics) [41]. TEM bright-field (BF) micrographs of irradiated samples were obtained. The size of the defects and defect densities were calculated based on these TEM images, especially from the peak damaged regions. Observations were conducted under a diffraction vector of $g = 200$ for BF and WBDF g-3 g imaging.

3. Results

3.1. RBS/C channeling

The RBS/C spectra were fitted using McChasy code, a Monte Carlo simulation package allowing the quantitative analysis of channeling spectra. A detailed description of RBS spectra analysis can be found in our previous study [30,32]. The materials responses (Ni, $Ni_{0.88}Fe_{0.12}$, $Ni_{0.77}Fe_{0.23}$, $Ni_{0.62}Fe_{0.38}$, $Ni_{0.38}Fe_{0.62}$) to the fluence of 4×10^{13} ions/cm^2 (□0.1 dpa), 2×10^{14} (□0.5 dpa), 1×10^{15} (□3 dpa) and 2×10^{15} ions/cm^2 (□6 dpa) are shown in Fig. 2A, B, C and D respectively. To facilitate an interpretation of the results, the reference "virgin" and "random" spectra are marked in the graph. The virgin spectra reflects undamaged crystal (the backscattering yield is low) while the “random” spectra correspond to the amorphous material (with a high level of lattice distortion). When the irradiation damage in the material appears, the backscattering yield is increasing. The variation of backscattering yield depends on the general lattice distortions in the implanted material. Therefore, we observe an increased backscattering yield with increasing lattice disorder.

For the fluence of 4×10^{13} ions/cm^2 the highest backscattering yield is visible for pure Ni, indicating an efficient defects accumulation in this material. In turn, for the fluences of 2×10^{14} and 1×10^{15} ions/cm^2 the level of lattice distortion is growing for all the compositions (visible an increased backscattering yield), however, for $Ni_{0.62}Fe_{0.38}$ and $Ni_{0.38}Fe_{0.62}$ yield is the lowest. At 2×10^{15} ions/cm^2, the spectra of pure Ni, $Ni_{0.77}Fe_{0.23}$ and $Ni_{0.62}Fe_{0.38}$ overlap which means, damage saturation for these compositions has been achieved, while $Ni_{0.38}Fe_{0.62}$ still remains the lowest. As we reported in our previous work [42] if the curves overlap, we are most likely dealing with similar defect sizes and similar densities. However, there are methods that can provide precise information on the size and density of defects, for example positron annihilation spectroscopy or doppler broadening spectroscopy. Detail description of these methods can be found here [43]. However, in our studies we provided only calculations based on TEM images as it also provide a reliable results. Moreover, it is worth emphasizing that Ni ions cause a significant lattice distortion at higher irradiation fluence (generating new defects and transforming from smaller to larger defects), which may lead to stress release and further affects the backscattering yield.

Interestingly, at the fluence of 1×10^{15} ions/cm^2 and 2×10^{15} ions/cm^2 an inverted intensity for $Ni_{0.77}Fe_{0.23}$ has been recorded at the depth of 320 nm. Such tendency could be related to a change in defect size. The shapes of the spectra up to the depth of 320 nm may indicate a predominance of point defects in $Ni_{0.77}Fe_{0.23}$. This also supported by TEM results (in Section 4). Next, the spectra of $Ni_{0.77}Fe_{0.23}$ and $Ni_{0.62}Fe_{0.38}$ overlap each other for the fluence of 1×10^{15} ions/cm^2 while at 2×10^{15} ions/cm^2 an inversed intensity region is formed (backscattering yield of $Ni_{0.77}Fe_{0.23}$ is lower than $Ni_{0.62}Fe_{0.38}$). This can be related to defects

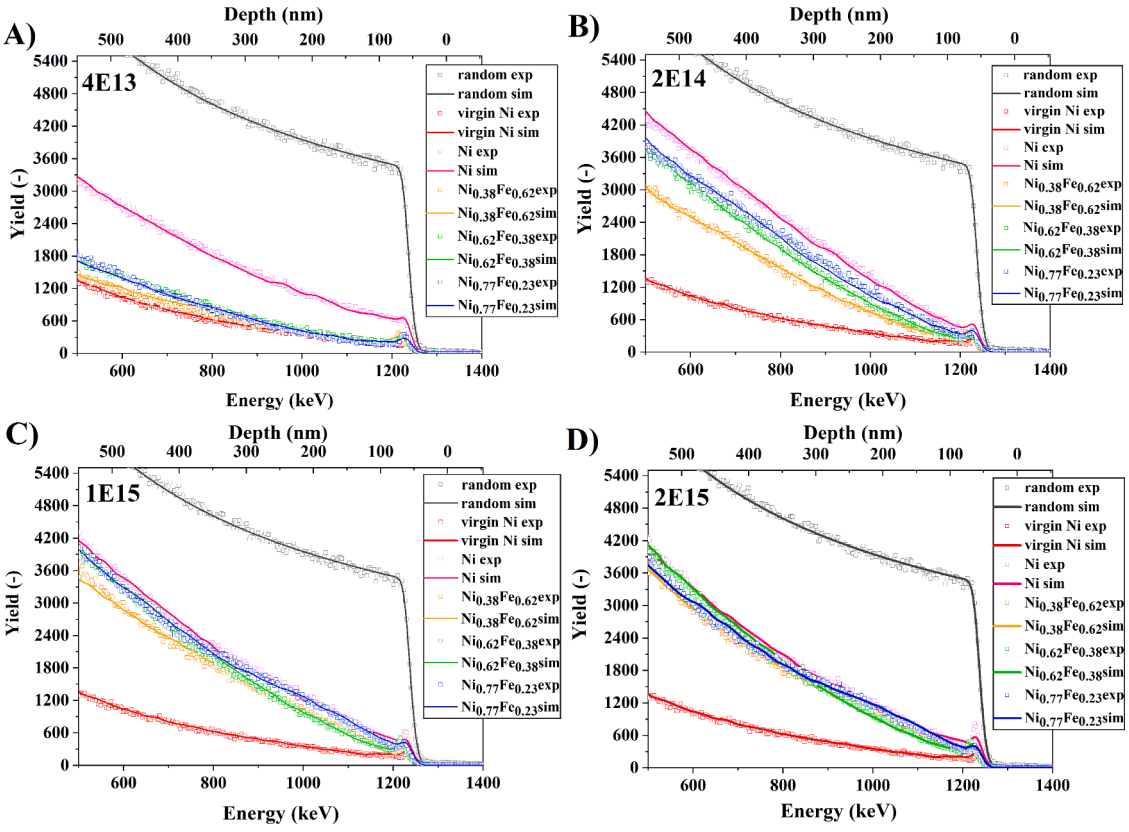

Fig. 2. RBS/C spectra of Ni and Ni_xFe_{1-x} single crystal samples irradiated with 1,5 MeV of Ni+ to the fluences of A) 4×10^{13}, B) 1×10^{15}, C) 1×10^{15} and D) 2×10^{15} ions/cm^2. The intensities of the spectra were normalized to the highest Ni-random spectrum.

agglomeration into bigger dislocation loops, which are further transformed into dislocation networks.

Fig. 3A-D shows the ion channeling spectra for pure Ni, $Ni_{0.77}Fe_{0.23}$, $Ni_{0.62}Fe_{0.38}$, and $Ni_{0.38}Fe_{0.62}$ submitted to ion irradiation. For the fluence of 4×10^{13} ions/cm^2, a significant decrease in the yield was observed for the binary alloys suggesting a suppression of defects accumulation with increasing Fe content. Above the fluence of 2×10^{14} ions/cm^2 (about 0.63 dpa), for pure Ni, we observe full saturation with defects. For the higher fluences (1×10^{15} and 2×10^{15} ions/cm^2 (□3 to 6 dpa respectively)), the yield decreases, which means that the material is fully saturated. In the case of $Ni_{0.77}Fe_{0.23}$ and $Ni_{0.62}Fe_{0.38}$, the saturation starts at the fluence of 1×10^{15}, while for $Ni_{0.38}Fe_{0.62}$ we notice a gradual yield build-up with ion fluence, which suggests there is still a room for damage to increase.

Usually, in metals, most of the defects are mainly extended defects, e.g., dislocations or stacking faults, which lead to the dechanneling of incident He ions [23]. It can be assumed that lattice distortion could be related to defect size and density change since smaller defects cause smaller lattice distortion than complex defects (defect cluster, dislocation), hence, backscattering yield changes. In pure Ni, a saturation dose has been obtained at a fluence of 2×10^{14} ions/cm^2. The saturation and a small decrease in channeling yield may occur because the defect structure becomes more organized at high fluence [44]. For example, point defects are transformed into more complex structures, such as dislocation loops, or small dislocation loops are changed into larger defect clusters that release strain induced by ion irradiation. Therefore, we observe a decrease in backscattering yield. Moreover, one can notice different compositions reach saturation at different fluences. This means that the defect evolution is delayed by adding more Fe to Ni. This is related to both defect generation and defect growth. Usually, at higher irradiation fluence the generation of new defects and transformation from smaller to larger defects may occur. Moreover, adding Fe may effectively influence the energy transport during ion irradiation through electrons on the defect formation and distribution [44].

3.2. Damage kinetics

The MSDA analysis was performed to reveal damage kinetics for investigated materials; Ni, $Ni_{0.77}Fe_{0.23}$, $Ni_{0.62}Fe_{0.38}$, and $Ni_{0.38}Fe_{0.62}$ and it is shown in Fig. 4. Points in the figure are corresponding to maximal values of extended defects formed in irradiated materials. Solid lines are the fits made following the MSDA equation [30,33,34]:

$$f_d = \sum_{i=1}^{n} \left(f_{d,\,i}^{sat} - f_{d,\,i-1}^{sat} \right) G\,[1 - \exp(\sigma_i(\Phi - \Phi_{i-1}))] \quad (2)$$

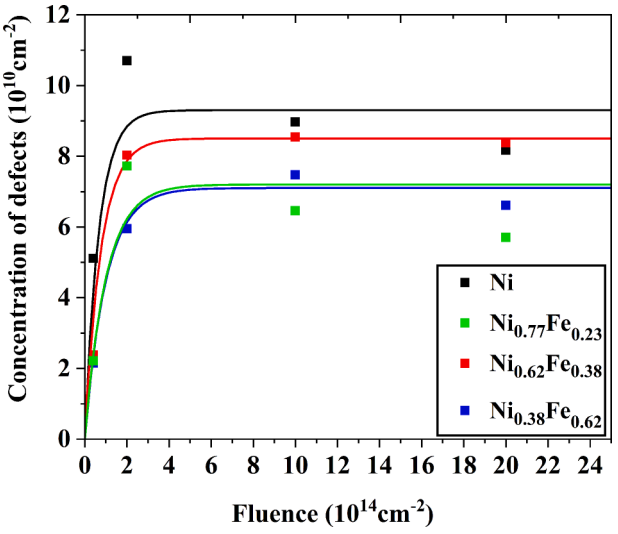

Fig. 4. Damage kinetics for all investigated materials. Points represent the maximal values of extended defect distributions extracted from McChasy simulations, solid lines are fits to the experimental data using the MSDA model.

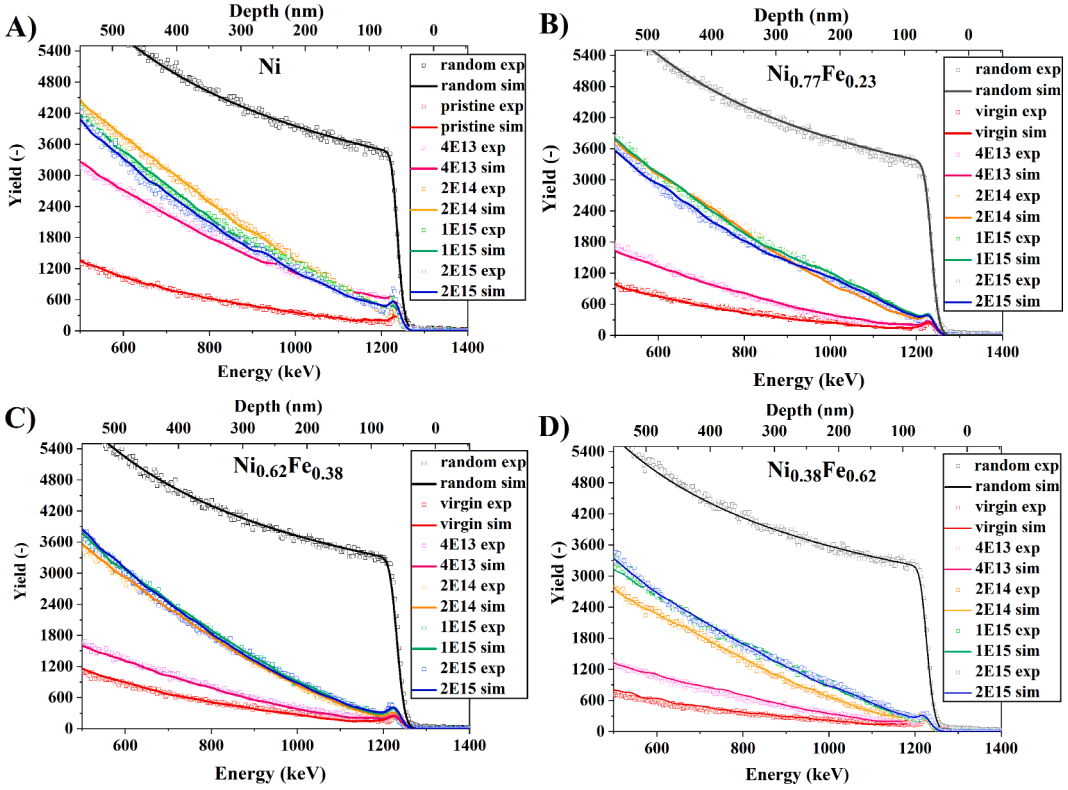

Fig. 3. RBS/C spectra of A) Ni, B) $Ni_{0.77}Fe_{0.23}$, C) $Ni_{0.62}Fe_{0.38}$, D) $Ni_{0.38}Fe_{0.62}$ single crystals irradiated with the fluences from 4×10^{13} to 4×10^{15} ions/cm^2. Solid lines represent fits obtained using MC simulations. Virgin and random spectra are included as references.

where:

σ_i - cross-section for the formation of a given kind of defect

$f_{d,i}^{sat}$ - level of damage at saturation for i-th kind of defects

Φ_i- fluence threshold for triggering the formation of i-th kind of defects

The decrease of cross-sections for defect formation for $Ni_{0.38}Fe_{0.62}$ and $Ni_{0.62}Fe_{0.38}$ alloys as compared to pure Ni single crystal is observed (see Table 1). The lower cross-section for damage formation $Ni_{0.38}Fe_{0.62}$ alloys suggests the suppression of defect accumulation. Interestingly, $Ni_{0.77}Fe_{0.23}$ shows a similar value of cross-section for defect formation as $Ni_{0.38}Fe_{0.62}$. This is most likely related to the fact that for the MSDA model, we used the extended defects only. As we observed in Fig. 2B, C and Fig. 3B, the shape of the spectra indicated the occurrence of point defects in $Ni_{0.77}Fe_{0.23}$ (up to the depth of 320 nm) in contrast to the rest of the tested compositions which is in line with MSDA calculations. As a result, the cross-section value for $Ni_{0.77}Fe_{0.23}$ is lower (indicated in Table. 1), since it consists of only extended defects and does not include the point defects contributing to the dechanneling level. Similar observation can be done for pure Ni structure. The consequence is a similar behavior of points in the MSDA model for Ni and $Ni_{0.77}Fe_{0.23}$ alloy, which differs from the next two compositions.

A rapid increase in the number of defects at 0.5 dpa (see Figs.2 and 3) has been noticed for all the compositions. The numbers of extended defects formed for low irradiation fluences are well below the values obtained for Ni. At higher irradiation fluences (1×10^{15} ions/cm^2 and 2×10^{15} ions/cm^2) one can observe a decrease in defect concentration. This effect suggests a transformation of small loops into larger loops or defect clusters. A higher number of smaller defect structures leads to a more pronounced lattice distortion in their vicinity, as compared to one large dislocation loop containing the same number of defects and, hence, more efficient dechanneling of the analyzing beam.

Finally, we would like to point out, since the results for the $Ni_{0.88}Fe_{0.12}$ composition practically coincided with $Ni_{0.77}Fe_{0.23}$, we did not include this composition in the RBS/C and MSDA studies to make the results more transparent.

3.3. Mechanical properties

Mechanical properties of Ni_xFe_{1-x} single crystal alloys have been evaluated using the nanoindentation technique. Indentation hardness as a function of contact depth for all the compositions is shown in Fig. 5A. It is seen that initial hardness is increasing up to 38 at% of Fe and then for 62 at% of Fe goes down below the hardness value of $Ni_{0.62}Fe_{0.38}$ but it is higher than $Ni_{0.77}Fe_{0.23}$. Moreover, one can notice the hardness values do not change with depth, which means we do not deal with the indentation size effect, therefore we can see almost flat curves. As we have already reported in our previous work [42] the possible reason for hardness change with the addition of the Fe element could be related to the phase transformations. Depending on the temperature and atomic percentage of Fe (Ni), different phases such as a stable $FeNi_3$ ($L1_2$), metastable FeNi ($L1_0$), and unstable Fe_3Ni ($L1_2$) phase can be formed in the binary FeNi alloys [45,46]. Since it is hard to detect such phases with XRD, in this study we conducted some atomistic MC/MD simulations to see different ordered phases in Ni_xFe_{1-x} alloys (Section 3.4).

Mechanical response to ion irradiation has been recorded by performing a series of multicycle indentations of the irradiated Ni and Ni_xFe_{1-x} alloys. The results for individual fluences and compositions are presented as the average hardness value obtained in the load range of 0.5–10 mN. However, when considering the ion-irradiated specimens, we look at hardness values only from a depth between 40 nm to 150 nm. This methodology allows minimization of the impact of unmodified bulk material. However, it may be slightly misleading and provides unnaturally elevated hardness results as the damage profile changes over depth (it is graded). However, according to the author's experience, a much deeper damage profile (probably generated with energies around 8 MeV) should be done to capture the graded nature of the ion-irradiated later. Fig. 5B shows the hardness as a function of irradiation fluence for pure Ni and Ni with 12, 23, 38, and 62 at% of Fe. It can be seen that the hardness growth with increasing ion fluences is visible for all of the tested materials. At first, a very rapid increase in the hardness occurs at the fluence of 4×10^{13} ions/cm^2 (□ 0.1 dpa) and then gradually grows up to the fluence of 5×10^{14} ions/cm^2 (about 1.5 dpa). Afterward, the increment in hardness slightly decreases for all the alloys, however, the trend stays maintained. The smallest increase in hardness with fluence has been observed for $Ni_{0.38}Fe_{0.62}$ and $Ni_{0.62}Fe_{0.38}$ samples, while the most drastic increase has been observed for Ni, followed by $Ni_{0.88}Fe_{0.12}$ and $Ni_{0.77}Fe_{0.23}$.

The Load-Displacement (L-D) curves obtained during multicycle indentation of irradiated *fcc* Ni, $Ni_{0.88}Fe_{0.12}$, $Ni_{0.77}Fe_{0.23}$ $Ni_{0.62}Fe_{0.38}$, $Ni_{0.38}Fe_{0.62}$ single crystal alloys at the fluences of 4×10^{13} ions/cm^2 and 4×10^{15} ions/cm^2 are presented in Fig. 5C and D, respectively. The hardness values in Fig. 5C-D originate from a depth of 100 nm. This probing depth allows for capturing relevant results, not distorted by artificial effects like, Indentation Size Effect (ISE) or indenter tip bluntness [47,48]. Therefore, to present the actual hardness values of the ion-implanted layer, taking into account the damage peak of about 400 nm (results estimated from SRIM) and the ISE effect, the analysis of the area from this region is sufficient to describe the behavior of the irradiated material.

Obtained data show that pure Ni (Fig. 5C-D) is the most sensitive to ion radiation as compared to other compositions. According to the results shown in the tables (Fig. 5C), it can be seen that the hardness at the fluence of 4×10^{13} ions/cm^2 (0.1 dpa) is increasing up to 23 at% of Fe element and then goes down for $Ni_{0.62}Fe_{0.38}$ and $Ni_{0.38}Fe_{0.62}$ respectively. The same trend appears for the fluence of 4×10^{15} ions/cm^2 (Fig. 5. D) (damage of □12 dpa) with higher hardness values, which suggests that the Fe element effectively suppresses irradiation damage. Importantly, the L-D curves show a similar trend in terms of the hardness values presented in Fig. 5A and B. As we pointed out above, the reason for the different mechanical response of the alloys after irradiation might be related to different arrangements of Fe atoms in a crystal structure resulting from the presence of different phases.

3.4. Hybrid MC/MD simulation

Fig. 6A shows the potential energy per atom with respect to the random distribution of atoms in the alloys as a function of the number of swap attempts normalized by the total number of atoms. It is seen from Fig. 6A that for $Ni_{0.77}Fe_{0.23}$ there is the highest drop in potential energy before convergence while for $Ni_{0.38}Fe_{0.62}$ the drop of energy is the least. This means that thermodynamically the random distribution for $Ni_{0.77}Fe_{0.23}$ is unstable. We analyzed the $L1_2$ and $L1_0$ structures during this process. In $Ni_{0.88}Fe_{0.12}$ alloy all the Fe atoms belong to $FeNi_3$ ($L1_2$) phase, which means the remaining Ni atoms are distributed in a form of clusters inside the matrix. As it is visible in Fig. 6B, after convergence of potential energy, for $Ni_{0.77}Fe_{0.23}$ most of the atoms (almost 70%) belong to the $FeNi_3$ ($L1_2$) phase, for $Ni_{0.62}Fe_{0.38}$, 19.8% of atoms belong to $FeNi_3$ ($L1_2$) phase, and for $Ni_{0.88}Fe_{0.12}$ 38% of atoms belong to $FeNi_3$ ($L1_2$) phase. We didn't observe the Fe_3Ni $L1_2$ structure for $Ni_{0.38}Fe_{0.62}$ alloy. In all four compositions, 1–3% of atoms belong to the $L1_0$ structure.

Table. 1
Cross-sections for defect formation extracted from the MSDA model.

	$\sigma_1(10^{-14}cm^2)$	$fd_1(10^{10}cm^{-2})$
Ni	1.5	9.3
$Ni_{0.77}Fe_{0.23}$	1.0	7.2
$Ni_{0.62}Fe_{0.38}$	1.3	8.5
$Ni_{0.38}Fe_{0.62}$	1.0	7.1

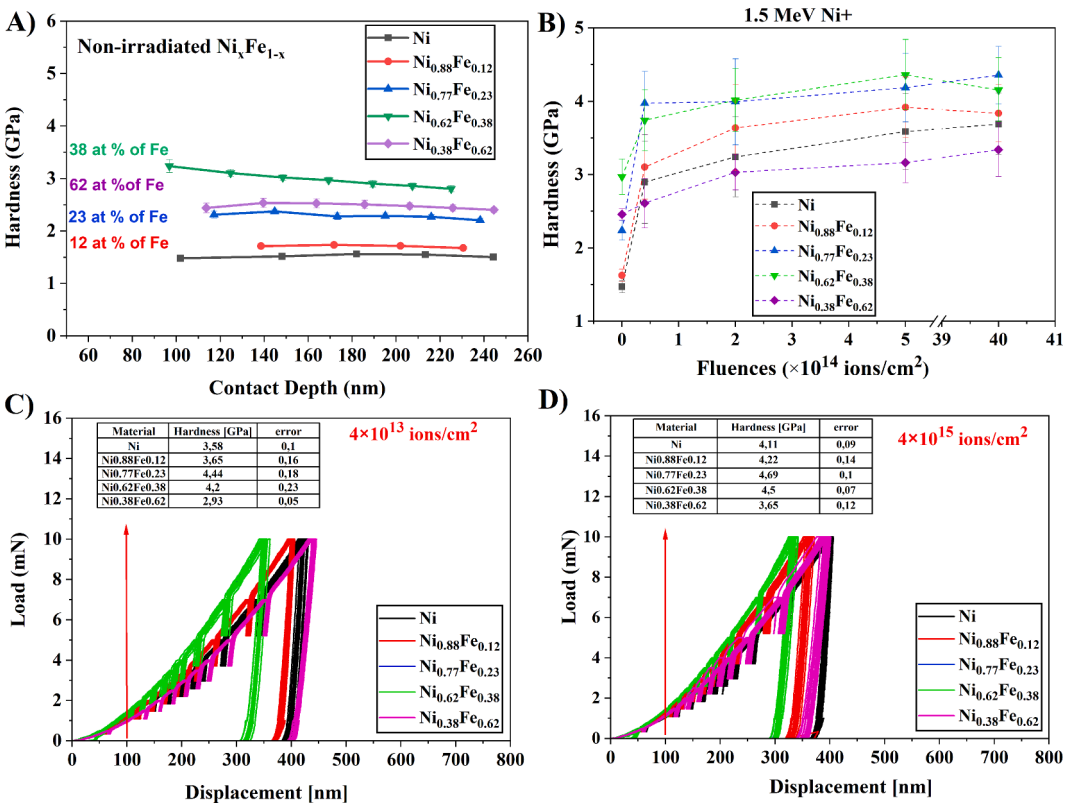

Fig. 5. A) Nanoindentation hardness of pristine *fcc* Ni, $Ni_{0.88}Fe_{0.12}$, $Ni_{0.77}Fe_{0.23}$ $Ni_{0.62}Fe_{0.38}$ and $Ni_{0.38}Fe_{0.62}$ single crystal alloys as a function of contact depth, B) Nanoindentation hardness of irradiated *fcc* Ni, $Ni_{0.88}Fe_{0.12}$, $Ni_{0.77}Fe_{0.23}$ $Ni_{0.62}Fe_{0.38}$ and $Ni_{0.38}Fe_{0.62}$ single crystal alloys as a function of ion fluences, Load-Displacement curves obtained during multicycle indentation of the irradiated *fcc* Ni, $Ni_{0.88}Fe_{0.12}$, $Ni_{0.77}Fe_{0.23}$ $Ni_{0.62}Fe_{0.38}$ and $Ni_{0.38}Fe_{0.62}$ single crystal alloys with the fluences of C) 4×10^{13} ions/cm^2 and D) 4×10^{15} ions/cm^2.

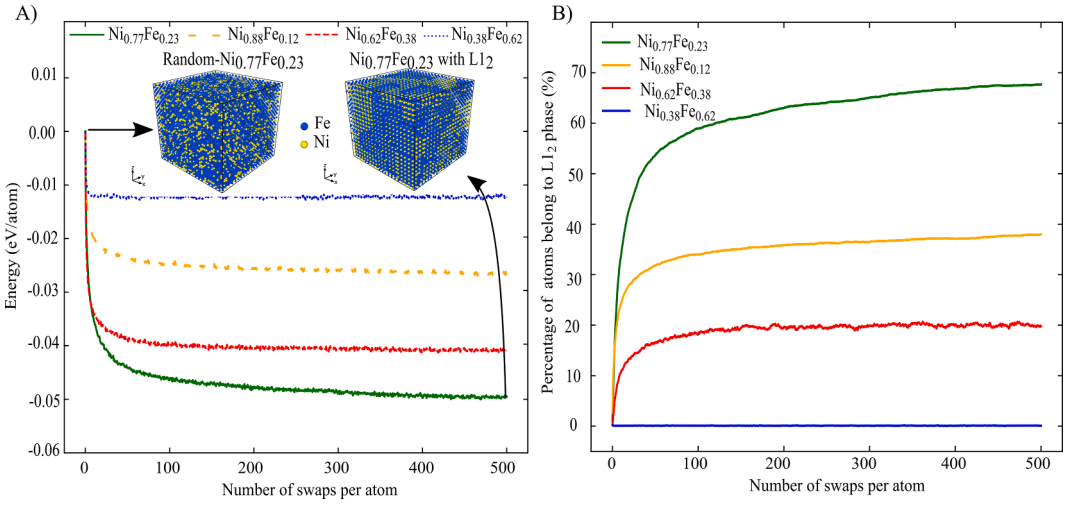

Fig. 6. A) the potential energy per atom with respect to the random case vs the number of swap attempts normalized by the total number of atoms for three different Ni_xFe_{1-x} binary alloys. B) Percentage of atoms belonging to $FeNi_3$ ($L1_2$) phase vs the number of swap attempts normalized by the total number of atoms for three different Ni_xFe_{1-x} binary alloys.

4. Discussion

To interpret the results based on atomistic simulations, we should notice that if nanoprecipitate with $L1_2$ phase is formed inside *fcc* alloys, the strength of the alloys will increase via the dislocation-bypass mechanism and dislocation-cutting mechanism [49]. This can be the main reason for the high hardness of $Ni_{0.62}Fe_{0.38}$ alloy, where around 20% of $L1_2$ atoms are formed in the disordered matrix. Although the $L1_2$ phase is also formed in $Ni_{0.77}Fe_{0.23}$ and $Ni_{0.88}Fe_{0.12}$ alloys, these two alloys showed less hardness before irradiation. For $Ni_{0.77}Fe_{0.23}$, most atoms are found in the $L1_2$ phase while the remaining belong to the disordered phase. Specifically, the disordered regions with randomly distributed Fe and Ni atoms are dispersed within the ordered $L1_2$ matrix. Consequently, the $L1_2$ phase cannot act as a nanoprecipitate and provide nanoprecipitate hardening prior to irradiation. In $Ni_{0.88}Fe_{0.12}$ alloy, all the Fe atoms belong to the $FeNi_3$ $L1_2$ phase, which means the remaining

Ni atoms are segregated inside the matrix. The hardness of $Ni_{0.88}Fe_{0.12}$ alloy is expected to be similar to that of pure Ni before irradiation. As irradiation can affect the distribution of Fe and Ni in the matrix, resulting in change of hardness, the impact of irradiation on the order-disorder phases will be investigated in the next study.

The irradiation-induced damage [50] can be categorized into two stages: primary and secondary. The primary damage occurs immediately after ion/neutron/electron impact by atomic collision processes far from thermodynamic equilibrium. The secondary damage is a long-timescale (nanoseconds to years) evolution caused by thermally activated processes [51]. During the secondary damage stage, the crystal defects evolve into more complicated microstructural features such as defect clusters, dislocation loops, and three-dimensional defects such as SFT [51]. Therefore, it is important to perform damage analysis at an early stage, e.g., 0.5 dpa and 12 dpa, to reveal defect evolution processes. For example, from hardness analysis, we have seen a drastic hardness increase in a low fluence regime up to 0.5 dpa. In turn, at higher fluences, the increase becomes less significant as the materials become saturated with defects. Therefore, in order to understand defect configurations in low and high fluence regimes, TEM analysis of each composition was conducted.

Fig. 7A shows cross-sectional TEM images of the Ni, $Ni_{0.77}Fe_{0.23}$, $Ni_{0.62}Fe_{0.38}$ and $Ni_{0.38}Fe_{0.62}$ irradiated with fluence of 2×10^{14} ions/cm^2 (damage level of 0.5 dpa), compared with SRIM calculations. The images were taken at a magnification of 150k in order to capture defects distribution below the sample surface. It should be emphasized, that all the lamellae have been cut perpendicularly to the ion-irradiated surface, to reveal the damage distribution into material up to the 2 um depth (in Fig. 7A, we show only the images up to 1100 nm). One can see that for Ni, $Ni_{0.77}Fe_{0.23}$ and $Ni_{0.62}Fe_{0.38}$ the damage zone reaches up to 600 nm (and it is in line with SRIM simulation where the damage peak is located at 400 nm), however, in $Ni_{0.38}Fe_{0.62}$ defects are evenly distributed and slightly exceeds a damage zone. Fig. 7B compares the TEM images of Ni, $Ni_{0.77}Fe_{0.23}$, $Ni_{0.62}Fe_{0.38}$ and $Ni_{0.38}Fe_{0.62}$ taken in a low fluence regime at 4×10^{13} ions/cm^2. The images come from the regions where the peak damage occurs in each alloy (taken at 500k magnification) to perform a detailed analysis of the defects and further to calculate the defect densities.

One can notice that defect concentration decreases as the iron content rises. In pure Ni, large defect clusters and dislocation loops are the dominant defect types. In $Ni_{0.77}Fe_{0.23}$, SFTs, defect clusters (relatively smaller than in Ni) and dislocation loops are clearly visible. In $Ni_{0.62}Fe_{0.38}$ and $Ni_{0.38}Fe_{0.62}$ SFTs, dislocation loops and clusters are mainly dominant.

Cross-sectional TEM images of the Ni, $Ni_{0.77}Fe_{0.23}$, $Ni_{0.62}Fe_{0.38}$ and $Ni_{0.38}Fe_{0.62}$ irradiated with a fluence of 4×10^{15} ions/cm^2 are shown in Fig. 8A. In contrast to the low fluence, in this case we see that the defects have moved significantly into the material and are outside the damage peak, calculated in the SRIM program. Interestingly, in Ni, $Ni_{0.77}Fe_{0.23}$ and $Ni_{0.62}Fe_{0.38}$ damage concentration is located at 700 nm, while in $Ni_{0.38}Fe_{0.62}$, the defects are evenly distributed from the surface into the material, similar to what we observed at low damage level (0.5 dpa in Fig. 7A). This phenomenon has been already reported in our previous work [42]. It was reported that the reason why a damage peak shift was observed in Ni_xFe_{1-x} at high fluence is that the ion irradiation causes high mechanical stress, where the ions may propagate toward the bulk of the material. As a result, we observe defect migration with an increased ion fluence as they generate a higher stress gradient due to the high amount of Ni ions implanted into the sample. Moreover, the migration mechanism could result from a combination of processes such as defect recombination, production, cluster formation etc. as reported in [3].

In Fig. 8B at the highest fluence (damage around 12 dpa) we can see the transformation of defect types in all the studied cases, which is consistent with RBS/C and MSDA analysis. For example, defects in Ni tend to form dislocation lines, SFTs, clusters, and dislocation loops while in $Ni_{0.77}Fe_{0.23}$ they form dislocation loops and STFs. In $Ni_{0.62}Fe_{0.38}$ and $Ni_{0.38}Fe_{0.62}$ we observe similar types of defects such as dislocation lines, many more SFTs, clusters and dislocation loops. It is known that the defect evolution proceeds as follows, first at low fluence point defects are transformed into clusters then into dislocation loops and stacking faults [52–54]. SFTs are known as the dominant type of defects in *fcc* NiFe single crystals having the shape of four equilateral vacancy-type stacking faults on {111} planes intersecting along <110> edges to form a perfect tetrahedron and are one of the most common vacancy-type defect clusters in metals of low stacking-fault energy [55].

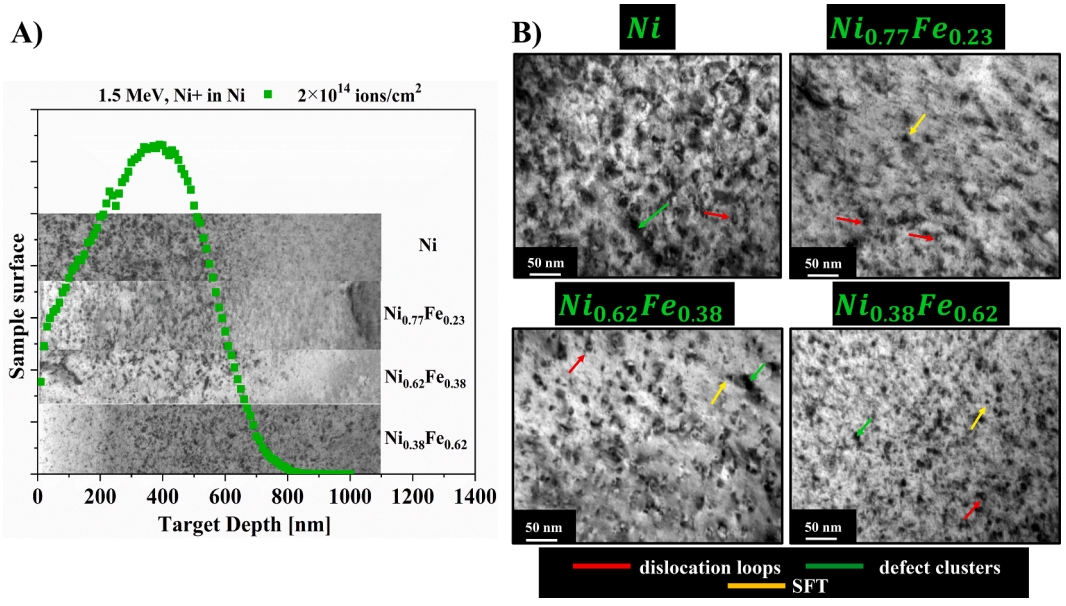

Fig. 7. A) Cross-sectional TEM images of the Ni, $Ni_{0.77}Fe_{0.23}$, $Ni_{0.62}Fe_{0.38}$ and $Ni_{0.38}Fe_{0.62}$ irradiated with a fluence of 2×10^{14} ions/cm^2 compared with SRIM calculations. B) Bright-field images of Ni, $Ni_{0.77}Fe_{0.23}$, $Ni_{0.62}Fe_{0.38}$ and $Ni_{0.38}Fe_{0.62}$ irradiated with a fluence of 4×10^{15} ions/cm^2. The red arrow indicates dislocation loops, green – defect clusters and yellow – SFT. (For interpretation of the references to colour in this figure legend, the reader is referred to the web version of this article.)

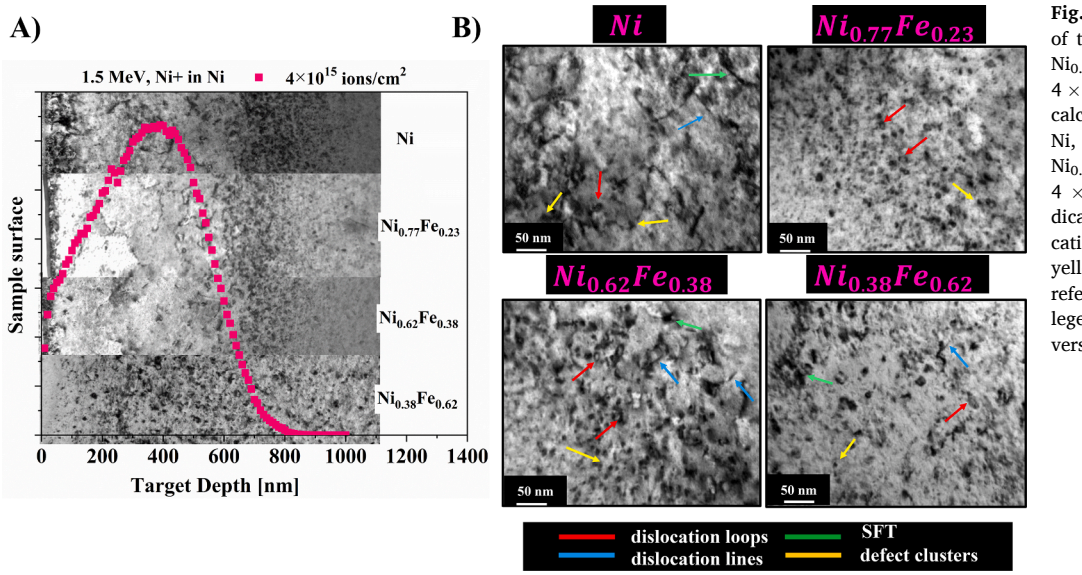

Fig. 8. A) Cross-sectional TEM images of the Ni, $Ni_{0.77}Fe_{0.23}$, $Ni_{0.62}Fe_{0.38}$ and $Ni_{0.38}Fe_{0.62}$ irradiated with a fluence of 4×10^{15} ions/cm^2 compared with SRIM calculations. B) Bright-field images of Ni, $Ni_{0.77}Fe_{0.23}$, $Ni_{0.62}Fe_{0.38}$ and $Ni_{0.38}Fe_{0.62}$ irradiated with a fluence of 4×10^{15} ions/cm^2. The red arrow indicates dislocation loops, blue – dislocation lines, green – defect clusters and yellow – SFT. (For interpretation of the references to colour in this figure legend, the reader is referred to the web version of this article.)

The vacancy-type SFTs can be produced in quenched metals or during irradiation by agglomeration of mobile vacancies at room and high temperatures [3], which significantly affects mechanical properties.

In addition, based on the defect sizes calculations presented in Fig. 9A, we can observe that in pure Ni damage propagates very fast up to 0.5 dpa (we see the biggest changes in the structure among the rest of the compositions). However, at about 12 dpa defects are re-organized, we can see elongated defect clusters or dislocation lines rather than big dot-shaped clusters. As shown in RBS/C spectra in Figs. 2 and 3, we observed that in the case of pure Ni defect saturation occurs above the fluence of 2×10^{14} ions/cm^2 (about 0.5 dpa). In $Ni_{0.77}Fe_{0.23}$, defects become bigger at the highest fluence and they are more organized in one region. In contrast, in $Ni_{0.62}Fe_{0.38}$ and $Ni_{0.38}Fe_{0.62}$ defects are constantly growing with fluence, which again is in line with RBS/C analysis, where we could see the continuous growth of backscattering yield. Furthermore, it is worth mentioning that the most meaningful changes are visible at a damage level of 0.5 dpa in each case. Moreover, as the damage level increases the defect sizes become bigger. This can be validated by calculations for individual composition based on TEM images, as shown in Fig. 9A. The defect size has been calculated as an average size of defects on the image (taken at the highest magnification, 500k) of the most degraded region (where the damage peak occurs). Fifty random defects (visible as black clusters) have been chosen to obtain useful statistics. Interestingly, defect sizes decrease with an increase in Fe up to 38 at% and for 62 at% of Fe accrue, both at low and high fluences. Additionally, for the highest dose (□12 dpa) the sizes of defects rise.

Moreover, in Fig. 9B defect densities have been calculated to better understand the defect configuration for various compositions. Calculations were made based on the TEM images taken at the peak damaged region (at the highest magnification of 500k). For this measurement, lamellae thickness was also measured at the peak damage region only. The densities were calculated by counting the defect sizes in a unit volume of crystalline material (based on the same image where an average defect size was calculated and presented in Fig. 8A). As a result, we can observe that the defect density values are inversely proportional to the defect size results for the individual chemical compositions. It can be seen that the defect densities increase for pure Ni and $Ni_{0.77}Fe_{0.23}$, while decrease for $Ni_{0.62}Fe_{0.38}$ and $Ni_{0.38}Fe_{0.62}$ for low fluencies. One can see that the size of defects decreases with the addition of iron. Usually, when irradiation damage increases, the dislocations disappear, and the density of the small interstitial-type loops or clusters increases [56]. Interestingly, the densities of network dislocations and dislocation loops increased with the irradiation dose. For this reason, these defects could work as defect sinks that could absorb the black spot damage. Therefore, more black spots would dissolve in the sinks when the network of dislocations and dislocation loops increased. Moreover, a part of the enlarged neighboring black spots may coalesce into more

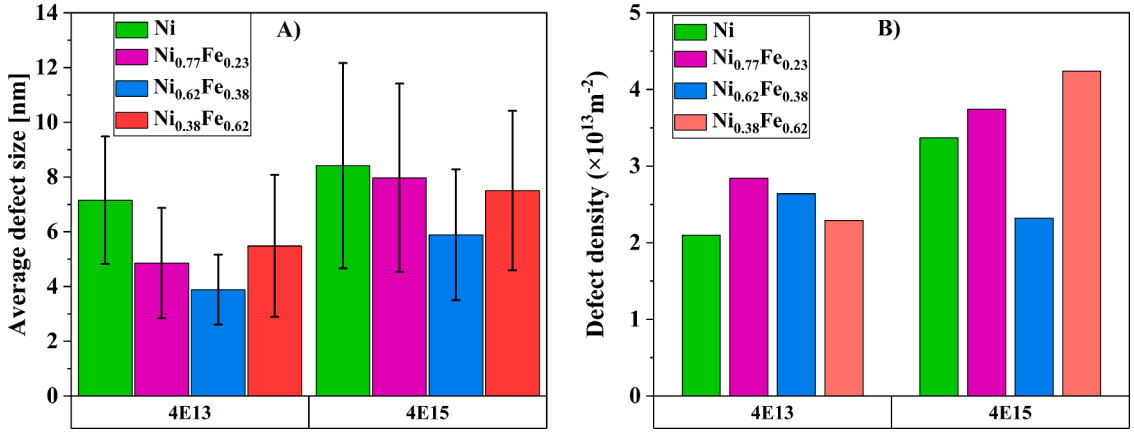

Fig. 9. A) Defect sizes based on the TEM images calculated at the fluence of 4×10^{13} ions/cm^2 and 4×10^{15} ions/cm^2 and B) Average defect densities for the Ni, $Ni_{0.77}Fe_{0.23}$, $Ni_{0.62}Fe_{0.38}$ and $Ni_{0.38}Fe_{0.62}$ irradiated to the fluence of 4×10^{13} ions/cm^2 and 4×10^{15} ions/cm^2.

prominent spots during irradiation, further decreasing their number [57,58]. While analyzing RBS/C spectra we have assumed that lattice distortion could be related to defect size and density change since smaller defects cause smaller lattice distortion as compared to complex defects (defect cluster, dislocation), hence, backscattering yield changes. In pure Ni, a saturation dose has been obtained at a fluence of 2×10^{14} ions/cm^2. The saturation and a small decrease in channeling yield occur because the defect structure becomes more organized at higher fluences, as we can see in Fig. 8A. We see that point defects are transformed into more complex ones, such as dislocation lines and larger defect clusters that release strain induced by ion irradiation. Therefore, we observe a decrease in backscattering yield. In order to better understand how the defect size would affect mechanical properties or RBS/C spectra we have introduced a detailed calculation of defect size up to around 20 nm at low and high fluence as shown in Fig. 10A and B. From the calculation, we can see that the smallest defects up to 5 nm occur in $Ni_{0.77}Fe_{0.23}$ and $Ni_{0.62}Fe_{0.38}$ in a low and high fluence regime. This is consistent with RBS/C results and MDSA analysis, which showed the existence of small defects (significantly more than the rest of the compositions) in the structure. It is clear that the size of defects increases at high fluence, which is in line with TEM images presented in Fig. 8A.

At high fluence we observe an increase in defect size for all the compositions, while in $Ni_{0.62}Fe_{0.38}$ defects are the smallest up to 10 nm. From MSDA analysis we assumed that in the case of high irradiation fluences such as 1×10^{15} ions/cm^2 and 2×10^{15} ions/cm^2 one can observe a decrease in defect concentration. This effect suggests a transformation in small loops into larger loops or defect clusters, which is visible in TEM images (Fig. 8A). We postulated that, the higher number of smaller defect structures leads to a more pronounced lattice distortion in their vicinity, as compared to one large dislocation loop containing the same number of defects hence more efficient dechanneling of the analyzing beam.

Furthermore, defect size and density could also affect the irradiation-induced hardening of the alloys. As we illustrate in Fig. 5B, the most prominent hardening occurred at low fluence regime in $Ni_{0.77}Fe_{0.23}$ where we deal with a significant transformation from small defects into bigger ones. Based on the results in Fig. 9B, we see that the average defect size decreases and the defect density increases. In contrast, $Ni_{0.62}Fe_{0.38}$ and $Ni_{0.38}Fe_{0.62}$ showed the lowest level of hardening among all the alloys. The reason behind such differences is most probably related to the physical nature of the iron atomic nucleus in its excited state (during irradiation), as it possesses only one orbital with unpaired electrons, while Ni has three orbitals. This could be explained, as Ni possesses more space for electron movements and, thus, defect generation and mobility [42]. Therefore, Fe effectively suppresses damage and stress induced by ion irradiation. The different arrangement of Fe atoms in a crystal structure may also influence the obtained characteristics of Ni_xFe_{1-x} after ion implantation, therefore, this should be validated by performing additional hybrid MC/MD simulation. In Fig. 5 we observed that the hardness of virgin materials is changing with the percentage of iron content. The preliminary results of MC/MD simulations (of virgin materials) have shown that depending on the iron content we achieved different structures. In $Ni_{0.77}Fe_{0.23}$, 70% of $FeNi_3$ ($L1_2$) phase is observed, while in $Ni_{0.62}Fe_{0.38}$ around 20%. $Ni_{0.38}Fe_{0.62}$ is characterized by disorder *fcc* structure. Moreover, simulations revealed that in each composition 1–3% of the $L1_0$ phase occurs. It is worth empathizing that, if the nanoparticipate $FeNi_3$ with $L1_2$ phase is distributed in the random *fcc* structure, the strength of the material increase [45,46]. It means that the material becomes harder. Therefore, in $Ni_{0.62}Fe_{0.38}$ we observe the maximum hardness in a pristine sample and then the hardness decrease in $Ni_{0.38}Fe_{0.62}$ where we deal with *fcc* phase and little amount of $L1_0$ phase (1–3%) according to simulations.

5. Conclusions

Comprehensive studies of *fcc* Ni_xFe_{1-x} single crystals were performed using a combination of various techniques to understand defect evolution and radiation response of each investigated composition. Ion channeling studies as well as damage kinetics demonstrated various responses of damage build-up mechanisms for each individual composition. We have noticed that the defect size and density influence the shape and intensity of the obtained RBS/C spectra depending on the composition. TEM images revealed a significant degradation of the structure at 0.5 dpa, especially for Ni and, the largest defects are observed at 12 dpa. From MSDA we observed a rapid increase in the number of defects at 0.5 dpa and a high increase in the dechanneling level observed in measured RBS/C spectra, for all the compositions. The numbers of extended defects formed for low irradiation fluences are well below the values obtained for Ni. At higher irradiation fluence of 1×10^{15} ions/cm^2 and 2×10^{15} ions/cm^2 we observed a decrease in defect concentration, which suggests a transformation of small loops into larger loops or defect clusters.

The atomistic simulations allowed to obtain insightful results related to hardening of Ni_xFe_{1-x} in a pristine state. The main reason for the highest hardness of $Ni_{0.62}Fe_{0.38}$ alloy before irradiation could be related to the presence of nanoprecipitate $FeNi_3$ ($L1_2$) phase (around 20%), which is formed inside the disordered matrix. It was found that a combination of atomistic simulations together with experimental studies may help to better understand mechanisms such as hardening and phase distribution within various Ni_xFe_{1-x} single crystals. Interestingly, irradiation can change the distribution of the atoms and increase the disordered phase, since irradiation may spread the Fe atoms inside Ni atoms and the hardness will increase. Therefore, as a next step, investigation of the hardening effect and verification of $L1_2$ phase presence

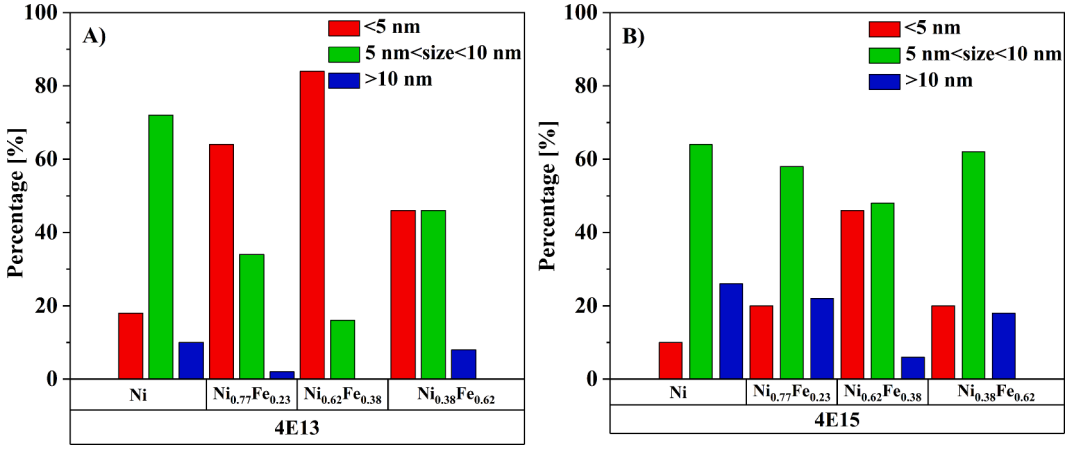

Fig. 10. Percentage of defect size obtained for A) low 4×10^{13} ions/cm^2 and B) high 4×10^{15} ions/cm^2 fluence up to 10 nm.

after irradiation in order-disorder phases should be performed. We postulate that the existence of the $L1_2$ phase influences the irradiation response of Ni_xFe_{1-x} single crystals.

Data availability

The data that support the findings of this study are available from the corresponding author, upon reasonable request.

CRediT authorship contribution statement

E. Wyszkowska: Conceptualization, Investigation, Writing – original draft, Writing – review & editing, Visualization. **C. Mieszczynski:** Writing – review & editing, Formal analysis, Investigation. **Ł. Kurpaska:** Writing – review & editing, Supervision, Formal analysis. **A. Azarov:** Investigation, Writing – review & editing. **W. Chromiński:** Investigation, Writing – review & editing. **I. Jóźwik:** Investigation, Writing – review & editing. **A. Esfandiarpour:** Investigation, Formal analysis, Writing – review & editing. **A. Kosińska:** Investigation. **D. Kalita:** Investigation. **R. Diduszko:** Investigation, Writing – review & editing. **J. Jagielski:** Formal analysis, Writing – review & editing, Supervision, Funding acquisition. **S.T. Nori:** Writing – review & editing. **M. Alava:** Formal analysis, Writing – review & editing.

Declaration of Competing Interest

The authors declare that they have no known competing financial interests or personal relationships that could have appeared to influence the work reported in this paper.

Acknowledgments

Financial support from the National Science Center, Poland through the PRELUDIUM 21 Program in the frame of grant no. 2022/45/N/ST5/02980 is gratefully acknowledged. This work was co-financed by the Polish Ministry of Education and Sciences through the project RaDeNiS (5003/LATR/2019/0). We acknowledge support from the European Union Horizon 2020 research and innovation program under NOMATEN Teaming grant agreement No. 857470 and from the European Regional Development Fund via the Foundation for Polish Science International Research Agenda Plus Program grant No. MAB PLUS/2018/8. The Research Council of Norway is acknowledged for the support of the Norwegian Micro- and Nano-Fabrication Facility, NorFab, project number 295864.

References

[1] N. Simos, H.G. Kirk, P. Thieberger, H. Ludewig, J.O. Conor, L. Mausner, et al., Irradiation damage studies of high power accelerator materials, J. Nucl. Mater. 377 (2008) 41–51.
[2] N. Anento, Y.O. A.Serra, Effect of nickel on point defects diffusion in Fe-Ni alloys, Acta Mater. 132 (2017) 367–373.
[3] C. Lu, K. Jin, L. Béland, et al., Direct observation of defect range and evolution in ion-irradiated single crystalline Ni and Ni binary alloys, Sci. Rep. 6 (2016) 19994.
[4] H.Bei K.Jin, Y. Zhang, Ion irradiation induced defect evolution in Ni and Ni-based FCC equiatomic binary alloys, J. Nucl. Mater. 471 (2016) 193–199.
[5] Mohammad W. Ullah, Dilpuneet S.Aidhy, Yanwen Zhang, William J. Weber, Damage accumulation in ion-irradiated Ni-based concentrated solid-solution alloys, Acta Mater. 109 (2016) 17–22.
[6] Ke Jin, Wei Guo, Chenyang Lu, Mohammad W. Ullah, Yanwen Zhang, William J. Weber, Lumin Wang, Jonathan D. Poplawsky, Hongbin Bei, Effects of Fe concentration on the ion-irradiation induced defect evolution and hardening in Ni-Fe solid solution alloys, Acta Mater. 121 (2016) 365–373.
[7] S.C. Middleburgh, D.M. King, G.R. Lumpkin, M. Cortie, L. Edwards, Segregation and migration of species in the CrCoFeNi high entropy alloy, J. Alloys Compd. 599 (2014) 179–182.
[8] A.F. Rowcliffe, L.K. Mansur, D.T. Hoelzer, R.K. Nanstad, Perspectives on radiation effects in nickel-base alloys for applications in advanced reactors, J. Nucl. Mater. 392 (2009) 341–352.
[9] S.J. Zinkle, G.S. Was, Materials challenges in nuclear energy, Acta Mater. 61 (2013) 735–758.
[10] Steven J. Zinkle, Jeremy T. Busby, Structural materials for fission & fusion energy, Mater. Today 12 (2009) 12–19.
[11] M. Frelek-Kozak, L. Kurpaska, M. Lesniak, I. Jozwik, J. Jagielski, Mechanical and structural properties of ODS RAF steels submitted to low-energy ions irradiation, Fusion Eng. Des. 127 (2018) 54–59.
[12] K. Vortler, G.Bonny N.Juslin, L. Malerba, K. Nordlund, The effect of prolonged irradiation on defect production and ordering in Fe-Cr and Fe-Ni alloys, J. Phys.: Condens. Matter. 23 (2011), 355007.
[13] W.R. Corwin, et al., The Gas Cooled Fast Reactor (GFR) Survey of Materials Experience and R&D Needs to Assess Viability, Oak Ridge National Laboratory Report ORNL/TM2004/99, Oak Ridge Tennessee, 2004.
[14] R.E. Stoller, L.K. Mansur, Modeling and Microstructural Analysis: Needs and Requirements for Generation IV Fission Reactors, Oak Ridge National Laboratory Report ORNL/TM-2003/242, Oak Ridge, Tennessee, 2004. May.
[15] G.O. Hayner, et al., Next Generation Nuclear Plant Materials Selection and Qualification Program Plan, Idaho National Engineering Laboratory Report INEEL/EXT-03-001128, Idaho Falls, Idaho, 2003 (Rev0)November.
[16] O.N. Senkov, G.B. Wilks, D.B. Miracle, C.P. Chuang, P.K. Liaw, Refractory high-entropy alloy, Intermetallics 18 (2010) 1758–1765.
[17] Z. Wu, H. Bei, F. Otto, G.M. Pharr, E.P. George, Recovery, recrystallization, grain growth and phase stability of a family of FCC-structured multi-component equiatomic solid solution alloys, Intermetallics 46 (2014) 131–140.
[18] Y. SG Ma, Zhang Effect of Nb addition on the microstructure and properties of AlCoCrFeNi high-entropy alloy Mat, Sci. Eng. A 532 (2012) 480–486.
[19] M.H. Chuang, M.H. Tsai, W.R. Wang, S.J. Lin, J.W. Yeh, Microstructure and wear behavior of $AlxCo_{1.5}CrFeNi_{1.5}Ti_y$ high-entropy alloys, Acta Mater. 59 (2011) 6308–6317.
[20] T. Egami, W. Guo, P.D. Rack, T. Nagase, Irradiation resistance of multicomponent alloys, Met. Mater. Trans. A 45 (2014) 180–183.
[21] Y. Zhang, G.M. Stocks, K. Jin, C. Lu, H. Bei, B.C. Sales, et al., Influence of chemical disorder on energy dissipation and defect evolution in nickel and Ni-based concentrated solid-solution alloys, Nat. Commun. 6 (2015) 8736.
[22] K. Jin, C. Lu, L.M. Wang, J. Qu, W.J. Weber, Y. Zhang, H. Bei, Effects of compositional complexity on the ion-irradiation induced swelling and hardening in Ni-containing equiatomic alloys, Scri. Mater. 119 (2016) 65–70.
[23] Leonard C. Feldman, James W. Mayer, S. Thomas Picraux, Materials analysis by ion channeling. Submicron Crystallography, Academic Press, 1982.
[24] Yanwen Zhang, Aurélien Debellec, Alexandre Boulled, Patrick Kluthe, Filip Tuomisto, Advanced techniques for characterization of ion beam modified materials, Curr. Opin. Solid State Mater. Sci. 19 (2015) 19–28.
[25] Modrzejewski, A., Metali, M. Wydawnictwo Naukowo-Techniczne, 1960.
[26] A. Saranraj, R. Murugan, S. Sahay Jude Dhas, M. Jose, S.A. Martin Britto Dhas, Indigenously developed vertical semi transparent Bridgman set-up for the growth of single crystals, Mater. Today Commun. 13 (2017) 386–390.
[27] Ziegler, J.F. SRIM-2013, www.srim.org.
[28] W.J. Weber, Y. Zhang, Predicting damage production in monoatomic and multi-elemental targets using stopping and range of ions in matter code: challenges and recommendations, Curr. Opin. Solid State Mater. Sci. 23 (2019), 100757.
[29] R.E. Stoller, M.B. Toloczko, G.S. Was, A.G. Certain, S. Dwaraknath, F.A. Garner, On the use of SRIM for computing radiation damage exposure, Nucl. Instrum. Methods Phys. Res. Sect. B Beam Interact. Mater. At. 310 (2013) 75–80.
[30] C. Mieszczynski, R. Ratajczak, J. Jagielski, G. Velişa, H. Bei, B.C. Sales, E. Wendler, W.J. Weber, Y. Zhang, Defect evolution in Ni and solid-solution alloys of NiFe and NiFeCoCr under ion irradiation at 16 and 300 K, J. Nucl. Mater. 534 (2020), 152138.
[31] J.Lian Zhang, Z. Zhu, W.D. Bennett, L.V. Saraf, J.L. Rausch, C.A. Hendricks, R. C. Ewing, W.J. Weber, Response of strontium titanate to ion and electron irradiation, J. Nucl. Mater. 389 (2009) 303.
[32] P. Jozwik, L. Nowicki, R. Ratajczak, A. Stonert, C. Mieszczynski, A. Turos, K. Morawiec, K. Lorenz, E. Alves, Monte Carlo simulations for ion channeling analysis of damage in dislocation-containing crystals, J. Appl. Phys. 126 (2019), 195107.
[33] J. Jagielski, L. Thomé, Multi-step damage accumulation in irradiated crystals, Appl. Phys. A 97 (2009) 147–155.
[34] J. Jagielski, L. Thomé, A. Chartier, O. Dorosh, C. Mieszczynski, I. Jozwik, Damage accumulation studies in ion-irradiated oxides: current status and new perspectives, Nucl. Instrum. Methods Phys. Res. B 435 (2018) 2–7.
[35] B. Sadigh, P. Erhart, A. Stukowski, A. Caro, E. Martinez, L. Zepeda-Ruiz, Scalable parallel Monte Carlo algorithm for atomistic simulations of precipitation in alloys, Phys. Rev. B 85 (2012), 184203.
[36] A. Esfandiarpour, R. Alvarez-Donado, S. Papanikolaou, M. Alava, Atomistic simulations of dislocation plasticity in concentrated VCoNi medium entropy alloys: effects of lattice distortion and short range order, Front. Mater. 9 (2022) 1–11.
[37] A.P. Thompson, H.M. Aktulga, R. Berger, D.S. Bolintineanu, W.M. Brown, P. S. Crozier, S.J. Plimpton, LAMMPS-a flexible simulation tool for particle-based materials modeling at the atomic, meso, and continuum scales, Comput. Phys. Commun. 271 (2022), 108171.
[38] C. Wu, B.J. Lee, X. Su, Modified embedded-atom interatomic potential for Fe-Ni, Cr-Ni and Fe-Cr-Ni systems, Calphad 57 (2017) 98–106, 2017.
[39] P.M. Larsen, S. Schmidt, J. Schiøtz, Robust structural identification via polyhedral template matching, Modell. Simulation Mater. Sci. Eng. 24 (2016), 055007.
[40] A. Stukowski, Visualization and analysis of atomistic simulation data with OVITO–the open visualization tool, Modell. Simul. Mater. Sci. Eng. 18 (2009), 015012.
[41] David B. Williams, C.Barry Carter, Transmission electron microscopy, A Textbook Mater. Sci. (2009) 352.

[42] E. Wyszkowska, C. Mieszczynski, Ł. Kurpaska, A. Azarov, I. Jóźwik, A. Kosińska, W. Chromiński, R. Diduszko, W.Y. Huo, I. Cieślik, J. Jagielski, Tuning heterogeneous ion-radiation damage by composition in Ni_xFe_{1-x} binary single crystals, Nanoscale 15 (2023) 4870.
[43] F.A. Selim, Positron annihilation spectroscopy of defects in nuclear and irradiated materials- a review, Mater. Charact. 174 (2021), 110952.
[44] Qingqing Ding, Yin Zhang, Xiao Chen, Xiaoqian Fu, Dengke Chen, Sijing Chen, Lin Gu, Fei Wei, Hongbin Bei, Yanfei Gao, Minru Wen, Jixue Li, Ze Zhang, Ting Zhu, Robert O. Ritchie, Qian Yu, Tuning element distribution, structure and properties by composition in high-entropy alloys, Nature 574 (2019) 223–227.
[45] G. Cacciamani, J. De Keyzer, R. Ferro, U.E. Klotz, J. Lacaze, P. Wollants, Critical evaluation of the Fe–Ni, Fe–Ti and Fe–Ni–Ti alloy systems, Intermetallics 14 (2006) 1312–1325.
[46] G. Cacciamani, A. Dinsdale, M. Palumbo, A. Pasturel, The Fe–Ni system: thermodynamic modelling assisted by atomistic calculations, Intermetallics 18 (2010) 1148–1162.
[47] Y.P. Sharkeev, E.V. Kozlov, The longe-range effect in ion implanted metallic materials: dislocation structures, properties, stresses, mechanisms, Surf. Coat. Technol. 158-159 (2002) 219–224.
[48] E. Wyszkowska, L. Kurpaska, M. Frelek-Kozak, I. Jozwik, K. Perkowski, J. Jagielski, Investigation of the mechanical properties of ODS steels at high temperatures using nanoindentation technique, Nucl. Instrum. Meth. B 444 (2019) 107–111.
[49] L. Liu, Y. Zhang, J. Han, X. Wang, W. Jiang, C.T. Liu, P.K. Liaw, Nanoprecipitate-strengthened high-entropy alloys, Adv. Sci. 8 (2021), 2100870.
[50] Gary S.Was, Funadametals of Radiation of Materials Science. Metals and Alloys, Springer, 2007.
[51] Kai Nordlund, Steven J. Zinkle, Andrea E. Sand, Fredric Granberg, Robert S. Averback, Roger E. Stoller, Tomoaki Suzudo, Lorenzo Malerba, Florian Banhart, William J. Weber, Francois Willaime, Sergei L. Dudarev, David Simeone, Primary radiation damage: a review of current understanding and Models, J. Nucl. Mater. 5012 (2018) 450–479.
[52] Jie Li, Xinhua Yang, Peng Wang, Qunli An, Healing stacking fault tetrahedron in NiFe solid solution alloys through grain boundary migration, J. Nucl. Mater. 565 (2022), 153738.
[53] Alexander Barashev, Yuri Osetsky, Hongbin Bei, Chenyang Lu, Lumin Wang, Yanwen Zhang, Chemically-biased diffusion and segregation impede void growth in irradiated Ni-Fe alloys, Curr. Opin. Solid. State. Mater. Sci. 23 (2) (2019) 92–100.
[54] Gihan Velișa, Mohammad W. Ullah, Haizhou Xue, Ke Jin, Miguel L. Crespillo, Hongbin Bei, William J. Weber, Yanwen Zhang, Irradiation-induced damage evolution in concentrated Ni-based alloys, Acta Mater. 135 (2017) 54–60.
[55] K. Nordlund, F. Gao, Formation of stacking-fault tetrahedra in collision cascades, Appl. Phys. Lett. 74 (1999), 2720-272.
[56] Dilpuneet S. Aidhy, Chenyang Lu, Ke Jin, Hongbin Bei, Yanwen Zhang, Lumin Wang, William J. Weber, Formation and growth of stacking fault tetrahedra in Ni via vacancy aggregation mechanism, Scri. Mater. 114 (2016) 137–141.
[57] H.C. Chen, D.H. Li, R.D. Lui, H.F. Huang, J.J. Li, G.H. Lei, Q. Huang, L.M. Bao, L. Yan, X.T. Zhou, Z.Y. Zhu, Ion irradiation induced disappearance of dislocations in a nickel-based alloy, Nucl. Instrum. Methods Phys. B 377 (2016) 94–98.
[58] S.X. Jin, L.P. Guo, Z. Yang, D.J. Fu, C.S. Liu, W. Xiao, R. Tang, F.H. Liu, Y.X. Qiao, Microstructural evolution in nickel alloy C-276 after Ar+ ion irradiation, Nucl. Instr. Meth. Phys. Res. B 269 (2011) 209–215.